



PYXIS: an integrated software package for synchrotron micro/nanodiffraction data analysis

Jiawei Kou and Kai Chen*

Center for Advancing Materials Performance from the Nanoscale (CAMP-Nano), State Key Laboratory for Mechanical Behavior of Materials, Xi'an Jiaotong University, Xi'an, Shaanxi 710049, People's Republic of China. *Correspondence e-mail: kchenbl@gmail.com

Received 16 October 2023

Accepted 13 January 2024

Edited by A. Borbély, Ecole National Supérieure des Mines, Saint-Etienne, France

Keywords: synchrotron X-ray Laue micro-/nanodiffraction; energy scans; zone-axis assisted indexing; peak position comparison; peak profile analysis.

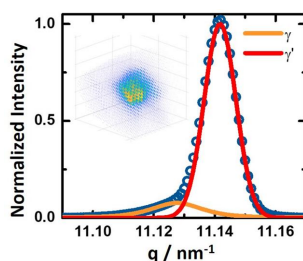
Supporting information: this article has supporting information at journals.iucr.org/j

PYXIS, a software package based on the MATLAB platform, is suitable for the in-depth analysis of synchrotron X-ray Laue micro/nanodiffraction and energy scan data. The main objective of the software is to analyze the following three aspects of the data. First, in a single Laue diffraction pattern, it can remove the background, search and index the peaks, and obtain the crystal orientation and the elastic strain tensor. A novel zone-axis assisted indexing algorithm has been developed to speed up this process. Second, a batch of Laue patterns obtained from a scan can be analyzed simultaneously to map the orientation and strain distributions, which is achieved efficiently by applying a peak position comparison strategy. An analysis of a Laue microdiffraction scan of the cross section of $\text{Li}_7\text{La}_3\text{Zr}_2\text{O}_{12}$ solid-state electrolyte has been taken as an example in this article to illustrate these functions. The third unique function in *PYXIS* involves data mining of energy scans. Considering a Ni-based superalloy as an example, the energy scan data sets are processed to reconstruct the diffraction peaks in three dimensions, allowing extraction of the lattice constants, lattice misfit and dislocation characteristics from the peak profiles.

1. Introduction

With the development of advanced synchrotron-radiation X-ray sources, X-ray focusing optics and large-area 2D X-ray detectors, synchrotron X-ray micro/nanobeam diffraction has emerged as a powerful materials characterization technique (Ice *et al.*, 2011). A typical micro/nano Laue diffraction experiment involves the focusing of a synchrotron polychromatic X-ray beam on a crystalline specimen. Once the X-ray beam size is smaller than, or similar to, the crystal grain size in the specimen, a Laue diffraction pattern will be generated and recorded by the 2D detector in less than 1 s. By raster-scanning the X-ray probe across the surface of the specimen, a large number of Laue patterns are collected, each of which reflects the crystallographic features of the scanned position (Ice *et al.*, 2005). By analyzing all these Laue patterns, information on the spatial distribution of phases (Dejoie *et al.*, 2014; Guo *et al.*, 2011; Mun *et al.*, 2011), crystal orientation (Ma *et al.*, 2015; Chen *et al.*, 2012; Wenk *et al.*, 2011), deviatoric lattice strain/stress (Chen *et al.*, 2015, 2020; Wenk *et al.*, 2020; Befus *et al.*, 2019), and microstructural defects like dislocations (Ohashi *et al.*, 2009; Tao *et al.*, 2019; Levine *et al.*, 2006) and twins (Chen *et al.*, 2011; Li *et al.*, 2015) can be mapped from the scanned area. However, analyzing thousands of Laue patterns simultaneously is non-trivial and an efficient data analysis tool is required for successfully interpreting the collected micro/nanodiffraction data.

To address the challenges associated with the inefficient analysis of Laue patterns, several software programs have



been developed at synchrotron beamlines, which include *XMAS* at the Advanced Light Source of Lawrence Berkeley National Laboratory (Tamura, 2014), *LaueGo* at the Advanced Photon Source of Argonne National Laboratory (Liu *et al.*, 2004), and *LaueTools* and its updated version *LaueToolsNN* at the European Synchrotron Research Facility (Robach *et al.*, 2014; Purushottam Raj Purohit *et al.*, 2022). Although these programs were designed for different beamlines, their primary functionalities, which involve peak identification, indexing, orientation and strain refinement, and peak profile study, are similar. With the computing clusters available at the beamlines, the efficiency of these software programs is acceptable. However, on an ordinary personal computer, analyzing a single Laue pattern takes several seconds (for the simple crystals such as Al, Cu) or up to several minutes (for some oxides with relatively larger unit cells), which is 10 to 1000 times more time consuming than data acquisition. With the increase in speed of 2D detectors, shrinkage in the X-ray beam size and increase in the flux of synchrotron radiation, the number of Laue patterns obtained from a typical micro/nanodiffraction scan is usually of the order of 10^3 to 10^5 . This leads to a considerable inflation in the processing time and calls for an improvement in the efficiency of the Laue pattern analysis. Since indexing is the slowest step in data processing, its speeding up is a priority (Örs *et al.*, 2018; Purushottam Raj Purohit *et al.*, 2022).

Furthermore, it is noted that only deviatoric strain tensors can be measured from Laue diffraction patterns. In some cases, the absolute value of the unit-cell parameters and/or the full strain tensors are needed, which necessitates the procurement of energy scans. In these experiments, a monochromator is inserted into the X-ray pathway to convert the polychromatic beam into a monochromatic one. By rotating the monochromator with fine steps, the energy of the monochromatic beam is selected correspondingly with small steps of a couple of eV. At each energy step, the diffraction signal is collected. Then, the energy profile of a Laue peak can be plotted (Zhou *et al.*, 2021). Therefore, exploring the functionality of data mining software packages for better utilization of the energy scan data can unlock a new paradigm in strain measurements.

In this paper, we introduce a custom-developed software package, *PYXIS*, which facilitates efficient analysis of Laue diffraction and energy scan data. *PYXIS* provides a user-friendly graphical interface with comprehensive functionalities that address the aforementioned challenges in diffraction data analyses. To improve the indexing efficiency, a zone-axis assisted indexing algorithm and peak position comparison strategy (Kou *et al.*, 2018) have been developed and incorporated into *PYXIS*. In this study, we will use these functions to map the orientation and strain distributions on the solid-state electrolyte $\text{Li}_7\text{La}_3\text{Zr}_2\text{O}_{12}$ (LLZO), a garnet-type crystal with a relatively large unit cell (Shen *et al.*, 2022). *PYXIS* can also reconstruct the 3D intensity distribution in the reciprocal space from experimentally obtained energy scan data, which further enables line profile analysis and measurement of lattice constants. Moreover, for crystals with semi-coherent

phases, peak profile decomposition can be achieved using *PYXIS* to calculate lattice misfit. To demonstrate this function, the data obtained from a Ni-based superalloy will be considered as an example case. The output of results analyzed by *PYXIS* can be input into our previously developed software package *XtalCAMP* (Li *et al.*, 2020) for further analyses and better visualization.

2. Technical description, availability and computing requirements

PYXIS has been developed on the MATLAB graphical user interface module and compiled into an executable file (.exe file). On Windows 7, 10 and 11 operating systems (32 bit or 64 bit), any version which is higher than MATLAB R2017b or correlated MATLAB Runtime must be installed to run the program. With the lower MATLAB versions, the program is still executable but might encounter some problems in image display. *PYXIS* has been registered at the Copyright Protection Center of China (registration No. 2021SR0152803). The software is available online at <http://nano.xjtu.edu.cn/info/1171/3455.htm>. *PYXIS* takes advantage of multithreading features built into MATLAB. Users can decide the number of computational threads by using either the default value, which is the maximum number determined by the hardware of the computer, or any other value smaller than the same.

3. Program functionalities and features

3.1. Basic functions and key features

PYXIS contains all functions required for common micro/nanodiffraction data processing. The primary modules and features are illustrated in Fig. 1. For single Laue pattern analysis, the functionalities include Laue peak/subpeak identification, peak indexing and orientation/strain refinement. To ensure efficiency, indexing could be executed using the conventional method or a zone-axis assisted indexing algorithm on a case-by-case basis. The Laue peaks can be studied in-depth by extracting the profile parallel or perpendicular to the peak streaking direction. For automatic batch analysis, Laue patterns can be processed either sequentially and independently or following the peak position comparison method, which not only provides higher efficiency but also explores the boundary of each individual grain more easily and accurately. For energy scan analysis, *PYXIS* can extract the intensities of a

Module	Single Laue Patterns	Batch Laue Patterns	Energy Scan Data
	<ul style="list-style-type: none"> Peak search Peak profile study Peak indexing Orientation/strain refinement 	<ul style="list-style-type: none"> Sequential analysis Peak position comparison strategy 	<ul style="list-style-type: none"> Reciprocal space reconstruction Line profile analysis
Feature	<ul style="list-style-type: none"> Subpeak identification & clustering Peak streaking analysis Zone-axis assisted indexing (ZAAI) Subgrain identification 	<ul style="list-style-type: none"> Multi-phase analysis Grain-by-grain analysis 	<ul style="list-style-type: none"> 3D peak separation Lattice constant/misfit measurement Dislocation density calculation

Figure 1
Basic functions and key features of *PYXIS*.

specific peak from a series of diffraction patterns taken with stepwise changed X-ray energy and then reconstruct them in the reciprocal space. If the peak is split, the intensities can be divided and assigned to each subpeak. Following the reconstruction, *PYXIS* can further integrate the intensities along a certain direction to generate a 1D profile for lattice constant measurement and dislocation density analysis.

PYXIS has unique features such as peak profile study in the \mathbf{q} space, a zone-axis assisted indexing algorithm for indexing, peak position comparison strategy for batch analysis, and lattice misfit and dislocation density measurements based on energy scan data reconstruction. These features will be illustrated with two examples, LLZO solid-state electrolyte and a Ni-based superalloy. Details of the sample preparation are described in Appendix A.

Laue patterns from a 2D cross section scan on a garnet-type LLZO polycrystal are analyzed step by step to show the high efficiency of *PYXIS*. The bulk LLZO solid-state electrolyte was assembled in a Li/LLZO/Li symmetrical cell. A cross section was mechanically fine-polished, and the sample was protected inside a sealed in-house-built sample stage purged with argon, with Kapton tape as the X-ray window. With the sample mounted on a high-resolution scanning stage tilted by 45° relative to the incident X-ray beam, a $300 \times 300 \mu\text{m}$ area including the interface of the LLZO electrolyte and the Li cathode was scanned with the micro-focused polychromatic (5–24 keV) X-ray probe with $2 \mu\text{m}$ scanning step size on Beamline 12.3.2 at the Advanced Light Source of Lawrence Berkeley National Laboratory. The interface was aligned with the vertical scan direction and closed to the left edge of the scanned region. A total of 22 500 Laue patterns were recorded in reflection mode with 0.1 s exposure using a 2D DECTRIS Pilatus-1M detector, which was seated about 150 mm above the X-ray focal point at 90° with respect to the incident X-rays.

The procedure of the energy scan data analysis is demonstrated by studying the lattice misfit in a heat-treated single-crystalline Ni-based superalloy and the dislocation density in its fatigue-tested counterpart. The superalloy single crystal mainly consists of two phases: the austenite phase γ -matrix and L_{12} -ordered γ' -Ni₃(Al, Ti, Ta) precipitates. The precipitates occupy $\sim 70\%$ of the volume fraction. A coarse dendritic structure is still visible after heat treatment because of the incomplete homogenization of the element segregation between the dendrite cores and the interdendritic regions. The primary dendrites are oriented approximately along the [001] direction, while the secondary dendrites are oriented along [100] and [010]. The misorientation between adjacent dendrites ranges from 1 to 5° . The energy scan experiment was carried out on Beamline 21A at Taiwan Photon Source. A Laue pattern was first acquired in the interdendrite area with the polychromatic (5–30 keV) X-ray nanoprobe, and then the monochromator was inserted into the X-ray pathway and the incident beam energy was scanned from 10023 to 10293 eV in steps of 2 eV. At each energy step, a diffraction pattern was recorded using a 2D DECTRIS Pilatus-6M detector with an exposure time of 0.1 s. The detector was installed about 520 mm above the X-ray focal point in reflection geometry.

3.2. Analysis of a single Laue pattern

3.2.1. Introduction to the main interface. The main interface of *PYXIS* provides common analysis functions for a single Laue pattern, as shown in Fig. 2. On the left side of the interface (Zone 1), a typical LLZO Laue pattern is displayed in false color, and different color styles can be chosen in the 'Display Set' toolbox. Users can also click on the pattern to enlarge a selected area in the 'Peak Mag' box (Zone 2), so that the shape of the peaks can be better observed.

Often, it is not enough to observe the diffraction peaks on the detector; it is also necessary to analyze them in the \mathbf{q} space (Ice & Barabash, 2007). To perform the coordinate system transformation, a detector coordinate system O - xy is established, in which the original position O is fixed at the top-left corner of the detector, the x and y axes are parallel with the horizontal and vertical edges of the detector, respectively, and the unit length equals the detector pixel size d_p . Any point P (x, y) on the detector is expressed by a vector \mathbf{k} that points from the X-ray focal point to P :

$$\mathbf{k} = \mathbf{A} \begin{bmatrix} (x - x_p)d_p \\ (y - y_p)d_p \\ 0 \end{bmatrix} + \begin{bmatrix} 0 \\ 0 \\ d \end{bmatrix}. \quad (1)$$

(x_p, y_p) are the coordinates of the projection position of the X-ray focal point on the detector, d is the focal point to detector distance, and \mathbf{A} is the transformation matrix defined by the rotation of the 2D detector:

$$\mathbf{A} = \begin{pmatrix} \cos \theta \cos \phi & \cos \theta \sin \phi & -\sin \phi \\ \cos \theta \sin \psi \sin \phi & \cos \theta \cos \psi \sin \phi & \cos \phi \sin \psi \\ -\cos \psi \sin \theta & +\sin \phi \sin \psi \sin \theta & +\sin \psi \cos \theta \end{pmatrix}^{-1}, \quad (2)$$

where θ , ψ and ϕ denote, respectively, the yaw, pitch and roll of the detector, and usually ϕ is set 0. For each pixel, P_i , on the 2D detector, its \mathbf{k} vector is denoted as \mathbf{k}_i . The incident X-ray beam is expressed as a unit vector \mathbf{k}_{in} in the detector coordinate system, and thus the scattering vector corresponding to

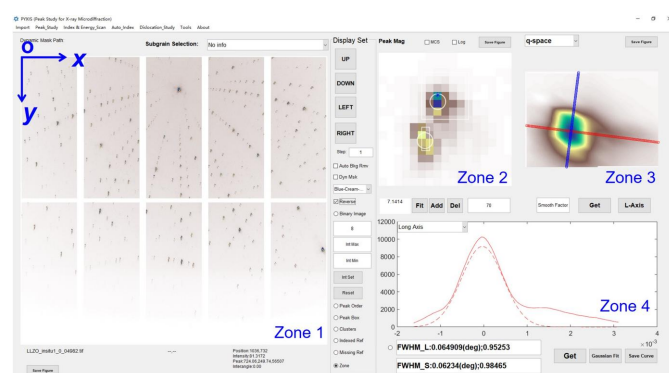


Figure 2
The main interface of *PYXIS*.

pixel P_i equals $\mathbf{k}_i - \mathbf{k}_{in}$. Then, all these scattering vectors are transformed into the \mathbf{q} space as $\mathbf{k}_{q,i}$:

$$\mathbf{k}_{q,i} = \mathbf{R}^{-1}(\mathbf{k}_i - \mathbf{k}_{in}). \quad (3)$$

\mathbf{R} is the transformation matrix from the detector coordinate system to the \mathbf{q} space:

$$\mathbf{R} = [\mathbf{x}_q \quad \mathbf{y}_q \quad \mathbf{z}_q]. \quad (4)$$

\mathbf{x}_q , \mathbf{y}_q and \mathbf{z}_q are the basis vectors of the \mathbf{q} space:

$$\mathbf{x}_q = \frac{\mathbf{k}_{in} \times \mathbf{k}_c}{|\mathbf{k}_{in} \times \mathbf{k}_c|}, \quad (5)$$

$$\mathbf{z}_q = \mathbf{k}_c - \mathbf{k}_i, \quad (6)$$

$$\mathbf{y}_q = \frac{\mathbf{z}_q \times \mathbf{x}_q}{|\mathbf{z}_q \times \mathbf{x}_q|}. \quad (7)$$

\mathbf{k}_c is the vector of the peak center, determined by fitting the diffraction peak using a Gaussian equation, which will be explained in Section 3.2.3. For Laue diffraction patterns, since the energy of all peaks is unresolved, the length of the corresponding scattering vector is also unknown. Thus the lengths of all \mathbf{k} vectors in equations (1) to (7) are normalized to unity, and $\mathbf{k}_{q,i}$ is scaled to $\mathbf{z}_q = 1$. The peak profile corresponding to the magnified image in the 'Peak Mag' window is projected onto the $\mathbf{z}_q = 1$ plane in the \mathbf{q} space and displayed in the window to the right (Zone 3).

To quantify the peak shape, the equivalent ellipse, which has the same second moments as the peak profile in the \mathbf{q} space, is defined. The long axis of the ellipse is parallel to the streaking direction of the peak, as displayed by the red line in Zone 3. The short axis is perpendicular to the long axis and marked by the blue line. The 1D Laue peak profile along either the long or the short axis is plotted (solid curve) and Gaussian fitted (dashed curve) in the window below (Zone 4). The fitted full width at half-maximum (FWHM) and coefficient of determination are shown below.

3.2.2. Typical procedure for single Laue pattern analysis.

Fig. 3 shows the typical procedure to analyze a single Laue pattern. Firstly, a Laue pattern is imported, as shown in Fig. 3(a). Then, the background which is mainly caused by fluorescence is removed and the peaks are identified. The peaks or subpeaks are marked by orange boxes and the subpeaks belonging to the same Laue peak are marked by cyan boxes [Fig. 3(b) with an inset, and this is why a cyan box may contain one or more orange boxes]. To apply the zone-axis assisted indexing algorithm, zone axes are identified on the basis of the searched peaks. The Laue peaks on the same zone axes are connected by blue dashed curves [Fig. 3(c)]. Finally, the Laue peaks are indexed, and next to each indexed peak its Miller indices are displayed in brown [Fig. 3(d)]. After indexing, refinement can be executed, and the orientation and strain results can be stored as isolated files. Stress can also be calculated if the stiffness tensor is known. A more detailed description of the Laue pattern analysis is provided in the following section.

3.2.3. Peak search. *PYXIS* removes the fluorescence background and identifies the peaks in the following approach. For a Laue pattern as shown in Fig. 3(a), the diffraction peaks are first erased using a median filter with the kernel size slightly larger than the peaks, and then the background is fitted using a median filter [Fig. 4(a)] (Arce & McLoughlin, 1987). By subtracting the background from the experimentally recorded Laue pattern, the peaks can be clearly visualized [Fig. 4(b)]. Afterwards, a threshold intensity I_a , which equals aI_{mean} , is employed to define peaks. Here I_{mean} is the mean intensity of all pixels on the Laue pattern after background removal and a is a user-defined parameter. In order to get rid of the influence of dead pixels, only the regions with intensities higher than I_a and larger than 2 pixels are treated as peaks. For easier description, the minimum rectangle that contains all connected pixels of the peak is called the peak territory. Two typical peaks, with their territories highlighted by rectangles, are displayed in the magnified zone in Figs. 4(c) and 4(d).

Accurate determination of peak positions is of top priority to secure the crystal orientation and lattice strain measurement accuracy. Therefore, the intensity profile in the rectangular territory is fitted using a 2D Gaussian distribution function to find the peak center coordinates (x_c , y_c). This method works well for the cases where a single peak is contained in the territory, as shown in Fig. 4(c). However, it must be taken into consideration that each peak territory may include more than one peak [Fig. 4(d)], caused by either the co-existence of slightly misoriented subgrains or the coincidence of different phases or grains in the X-ray irradiated

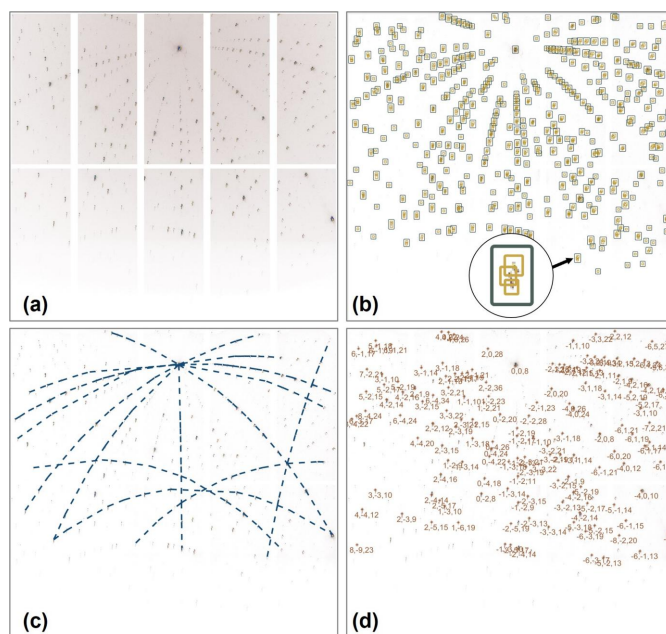


Figure 3
A step-by-step procedure for single Laue pattern analysis. (a) A typical Laue pattern taken on LLZO. (b) Diffraction peaks searched on the Laue pattern. (c) Zone axes identified from the searched peaks. (d) Miller indices of the indexed Laue peaks.

specimen volume. For these cases, peaks in the same territory need to be separated prior to peak position determination.

Thus, a new algorithm was developed. First, the difference in intensity of the threshold I_a and the highest intensity in any peak territory I_{\max} is denoted as H . *PYXIS* allows users to input a parameter n , with which H will be evenly divided into n parts, with the boundary intensities of $[I_a + (1/n)H]$, $[I_a + (2/n)H]$, $[I_a + (3/n)H]$, ..., $[I_a + (n-1/n)H]$. Taking the peak territory in Fig. 4(e) as an example, in which n is set to 3, the peak profiles are checked against the intensity values of $[I_a + (2/3)H]$ and $[I_a + (1/3)H]$ sequentially from high to low intensity. For the $[I_a + (2/3)H]$ intensity level, two subpeaks (marked as P1 and P2) are isolated [Fig. 4(f)]. On considering the intensity level one layer below, on the $[I_a + (1/3)H]$ level, the peaks that overlap with P1 and P2 are ignored, while a third peak, P3, shows up. Therefore, inside the peak territory in Fig. 4(e), three peaks are found, each of which will be fitted using a 2D Gaussian distribution function: two on the intensity level of $[I_a + (2/3)H]$ and the third on $[I_a + (1/3)H]$. The same practice will be executed on all the peak territories in the Laue pattern using the same parameter n .

It is obvious that the number of subpeaks searched and fitted, as well as the time consumed on this process, depend on the user-defined parameter n . A larger n ensures that more peaks are identified and accurately measured, with the caveat that it will also take a longer time. Empirically, for crystals with relatively poorer plasticity like ceramics and intermetallics, a value between 3 and 5 is suggested, while for ductile materials such as metals and alloys, a larger n , 8–10, is usually more suitable. It is not encouraged to set n to a value > 10 , as it leads to the misinterpretation of noise signals as diffraction peaks,

which in turn leads to unsuccessful indexing of the Laue pattern.

3.2.4. Peak indexing and orientation/strain refinement. The basic algorithms for automated Laue diffraction pattern indexing and orientation/strain refinement have been established by Chung & Ice (1999). In their method, all experimentally recorded Laue peaks are converted into scattering vectors \mathbf{k}_i , and the angle between each pair of scattering vectors (\mathbf{k}_i and \mathbf{k}_j) is calculated and denoted as τ_{ij} . Simultaneously, based on the user-input candidate crystal structure and its lattice constants (a , b , c , α , β , γ), a look-up table is established, which contains all possible angles (τ_{ij}) between each pair of crystallographic plane normals (except the extinction ones). The best match of the experimental angle list and the look-up table provides the correct Miller indices for each Laue peak and the crystal orientation. Subsequently, following the Nelder–Mead simplex approach (Olsson & Nelson, 1975), the symmetry restriction of the given crystal structure is eased by varying a/c , b/c , α , β and γ , until the minimum deviation between the experimental observed scattering vector directions and the calculated ones is achieved. By comparing the refined lattice constants and the theoretical ones, the deviatoric lattice strain is obtained (Chung & Ice, 1999). More details on strain refinement can be found in Appendix B. By clicking ‘Calculate Stress Tensor’ in the ‘Tools’ drop-down menu on the main interface (Fig. 2), the stiffness tensor can be loaded, which enables stress tensor calculation by applying Hooke’s law. To further improve the analysis efficiency, the following strategies are developed in *PYXIS*.

First, to speed up the indexing process, *PYXIS* clusters the subpeaks that split from the same Laue peak and indexes them as an assembly. In practice, a threshold value δ is input by users, and then if the angle between the scattering vectors of two peaks is smaller than δ , these two peaks are regarded as subpeaks belonging to the same peak. The selection of the threshold value δ needs to consider the materials properties and deformation status. Usually δ is set to be 0.5° or lower for ceramics and 1.0° for metals. Sometimes more than two subpeaks will be grouped into one peak. Such subpeak groups, for simplicity, will be called virtual peaks in this study. The position and intensity of a virtual peak are defined to be the intensity-weighted center and the summation of all the subpeaks belonging to it, respectively. Because the subpeaks in a virtual peak have the same Miller indices, it will be much faster to index a Laue pattern composed of all virtual peaks than to index only one subpeak at a time. After indexing the virtual peaks, accurate orientation and strain measurement of each subgrain is achieved by refinements based on subpeaks. Since the refinements are always much faster than indexing, the overall time consumed for Laue pattern analysis is effectively reduced.

The second feature in *PYXIS* is the zone-axis assisted indexing algorithm which significantly accelerates indexing. Taking the Laue pattern shown in Fig. 5(b) as an example, a total number of 398 peaks are searched. After each peak has been converted into a scattering vector as explained in

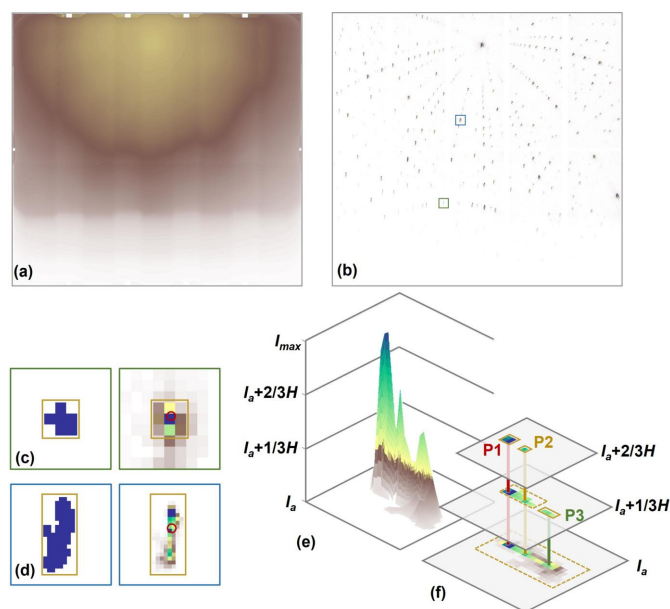


Figure 4

Peak search procedure employed by *PYXIS*. (a)–(b) show a typical Laue pattern before and after background subtraction. Laue peaks without and with splitting are magnified and displayed in (c)–(d). (e)–(f) demonstrate the identification of subpeaks schematically.

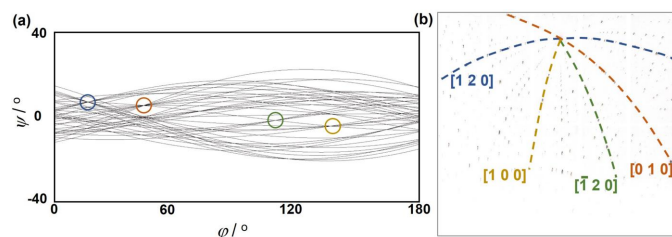


Figure 5

Schematics of the zone-axis assisted indexing of Laue patterns. (a) Zone axes are identified as the intersections of great circles that are perpendicular to the scattering vectors. (b) By indexing the zone axes, the crystal orientation can be obtained.

Section 3.2.1, the plane perpendicular to each of the scattering vectors and passing through the unit sphere's center point is calculated. The intersection of such a plane and the unit sphere surface is the great circle corresponding to the scattering vector. To visualize the great circles with greater clarity, they are plotted in a ψ - ϕ coordinate system, in which the ψ and ϕ axes are parallel to the longitudinal and latitudinal directions of the unit sphere, respectively. In Fig. 5(a), the great circles corresponding to 40 peaks with the highest intensity among the searched 398 peaks are plotted. In practice, all these 398 peaks will be converted into great circles. By applying the generalized Hough transformation (Ballard, 1981), the great circle intersections, which represent the zone axes, are identified. Four zone axes are picked up in Fig. 5(a), which are also marked as dashed curves on the Laue pattern in Fig. 5(b), with colors consistent with each other. In a real application, the great circles of all the 398 peaks are counted and 40 zone axes are found. Once the zone axes have been found, the angle between any pair of them is measured. These measured zone-axis angles are then compared with the computed ones based on the candidate crystal structure, and the best fit gives the $[uvw]$ of each zone axis [such as those marked in Fig. 5(b)] as well as the crystal orientation of the Laue pattern. Subsequently, the crystal orientation is further refined with all the peaks to acquire Miller indices of each peak and to improve the accuracy of orientation measurement, which is essential for strain measurement. It is noticed that although the zone-axis assisted indexing strategy requires two more steps of zone-axis identification and orientation refinement, it is much faster than the conventional method.

3.3. Batch analysis of Laue patterns

All the functions described above for the single Laue pattern analysis are also available for automatic batch analysis. Moreover, the user has the option of two serial strategies. One is a conventional sequential analysis, in which Laue patterns are analyzed one by one from the lowest number to the highest. The other is called the peak position comparison method, which was developed by our research team (Kou *et al.*, 2018). With this method, the batch analysis can be accelerated, and it becomes more convenient to investigate the scanned sample area in a grain-by-grain manner and to

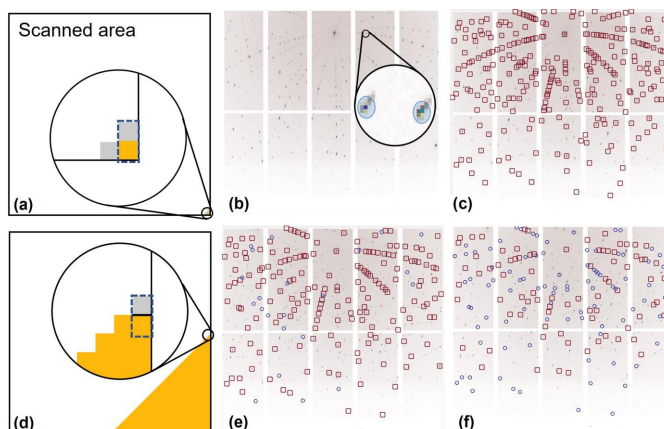


Figure 6

Scheme of the peak position comparison strategy for batch analysis of Laue scans. (a) The first pattern location. (b) Tolerance region associated with each indexed Laue peak. (c) The adjacent Laue pattern, with all peaks falling in the tolerant regions. (d) Location near the grain boundary. (e) The Laue pattern in the grain, with most peaks falling in the tolerant regions. (f) The Laue pattern out of the grain, with more than 50% of peaks falling out of the tolerant regions.

visualize the grain boundary zones more clearly. In the following, a 2D scan on the cross section of a garnet-type LLZO sample [space group $Ia\bar{3}d$, lattice constant $a = 1.2957$ nm (Yu *et al.*, 2016)] is studied using the peak position comparison method.

First, the first Laue pattern of this scan is imported into *PYXIS*, and then the routines for conventional individual Laue pattern analysis are applied, including indexing and refinement to obtain its orientation and strain. In this experiment, the scan has been performed from right to left and from bottom to top; thus the first Laue pattern corresponds to the bottom-right pixel in the scanned area, indicated by the orange block in Fig. 6(a). In this pattern, a total of 197 peaks are successfully indexed using the zone-axis assisted algorithm. Subsequently, an area of tolerance is calculated for each of the indexed peaks, marked by the blue ellipses in the enlarged view in Fig. 6(b). The definition of the tolerance ellipses is similar to the parameter δ introduced in Section 3.2.4 that is used for the subpeak grouping process. In the example here, the ellipses are generated on the basis of a tolerance value of 0.15° surrounding each peak. Then the Laue patterns collected at the adjacent positions, the gray ones to the left and on top, are imported into *PYXIS* sequentially to compare with this indexed one. The pattern taken at the top neighboring position is shown in Fig. 6(c). On this pattern, all the 197 tolerance ellipses are occupied with searched peaks (marked using red boxes). Hence the Miller indices obtained from the previous pattern will be directly assigned to the new pattern without 'really' indexing it, and then refinements are carried out to get the accurate local orientation and strain. The Laue pattern taken at the left scanning position is analyzed following exactly the same procedures, and it is found that the left position is also from the same crystal grain. Afterwards, tolerance ellipses are calculated for the upper and left patterns, respectively, and then compared with their neighbors.

This ‘comparison, assignment and refinement’ procedure will be executed repeatedly, until the boundary of this crystal grain is figured out, as shown in Fig. 6(d). At the orange pixel appearing in the dashed blue box, the Laue pattern [Fig. 6(e)] looks similar to those in Figs. 6(b) and 6(c); 175 tolerance ellipses, out of 197, are occupied by peaks and thus exhibit the same orientation as the first pattern. However, in the Laue pattern taken at the gray pixel just on top of it, only 82 peaks enter the tolerance ellipses [Fig. 6(f)], occupying merely 42% of the total tolerance ellipse. By default, grain boundaries are discerned if less than 50% of the total tolerance ellipses are occupied by peaks. Therefore, the gray pixel is judged to be a different crystal grain from the one at the bottom-right corner. It is noted that the grain boundaries might shift if a different threshold value (lower or higher than 50%, such as 30% or 70%, of the total number of tolerance ellipses) is employed, but the discrepancy is always no more than 2 pixels. Hence the difference is ignored. Once the territory of an ‘old’ grain has been fully mapped and a new grain is reached, the indexing, refinement and comparison procedures of the new grain will be performed in the same way, until all the Laue patterns, and thus the whole scanned area, has been studied.

Practically, any diffraction pattern from a Laue scan can be chosen as the first one to index, not necessarily the one taken at the corner.

Fig. 7(a) shows the inverse pole figure orientation map along the x axis of the scanned LLZO cross section. Three crystal grains (G1 to G3) have been identified, and in the border areas two or three grains can be indexed in a Laue pattern. Gray pixels correspond to the Laue patterns that could not be indexed, while the blank area to the left of the scan is out of the LLZO crystals. Fig. 7(b) shows the normal strain tensor components (the diagonal elements of the deviatoric lattice strain tensors) for each of the three grains separately. High strains are observed near the interface between the LLZO electrolyte and lithium electrode, whereas no strain concentration is detected near the grain boundaries in the bulk electrolyte.

The zone-axis assisted indexing algorithm and peak position comparison serial strategy can be used together to speed up the analysis. However, there are caveats associated with both strategies. For instance, for Laue patterns obtained from

crystals with small unit cells, in which a limited number of peaks are collected, zone-axis assisted indexing may not function well. Similarly, the peak position comparison strategy is challenging when a Laue scan is carried out with a large step size which leads to a significant difference in the crystal orientation between two adjacent scanning positions.

3.4. Analysis of energy scan data

3.4.1. Peak reconstruction. Batches of energy scans can be analyzed using *PYXIS*. In each scan, the synchrotron X-ray beam irradiates the specimen at a fixed position, while a series of diffraction patterns is taken at various, usually continuously changing, energies with a constant energy step size, and the intensity of the incident X-ray beam is also recorded. Between different energy scans, the irradiation position probably changes. Although the data format varies from beamline to beamline, the principle is similar. In the following, an example collected on Beamline 21A at Taiwan Photon Source is shown.

By clicking ‘Energy Scan Pattern Analysis’ in the ‘Index & Energy_Scan’ drop-down menu on the main interface (Fig. 2), the ‘Energy Scan Pattern Analysis’ interface is activated, as displayed in Fig. 8. One of the diffraction patterns in the energy scan batch, as well as the text file containing the experimental log information, is loaded in Zone 1. The text file name follows the format of ‘ t_{n_1} ’ and the pattern follows ‘ $t_{n_1-n_2}$ ’, where the text t is input by users, the number n_1 indicates the sample location and the number n_2 indicates the energy scan step (corresponding to a certain energy). Users can use the ‘E+/-’ and ‘P+/-’ buttons to switch between different X-ray energies and sample locations. Users need to click on the pattern in Zone 2 to select the area of interest, which is usually the location on the detector where the diffraction peak appears. The selected area is magnified in Zone 3 on the right. The magnification can be changed by inputting different values in the dashed ellipse to determine the area for peak study.

PYXIS can convert the selected areas of all the patterns in an energy scan into the reciprocal space and reconstruct the diffraction peaks contained in the volume of interest in three

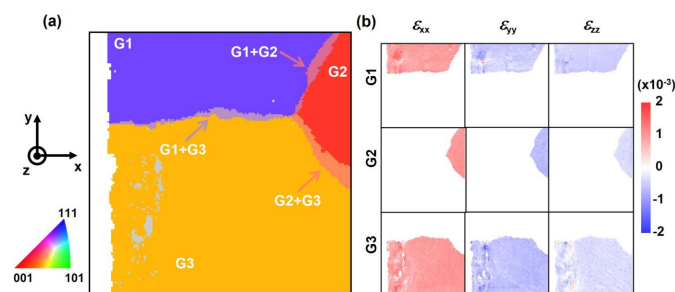


Figure 7
Microstructure mapping of the LLZO specimen obtained from Laue scan data analyzed using *PYXIS*. (a) Inverse pole figure map along the x axis. (b) A grain-by-grain analysis of the residual strain distribution.

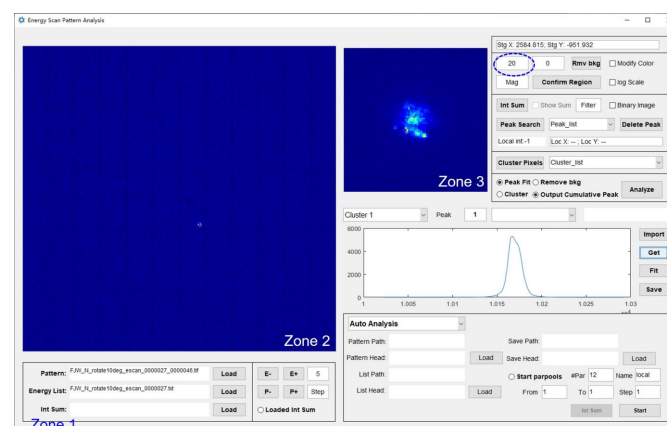


Figure 8
The interface for energy scan pattern analysis.

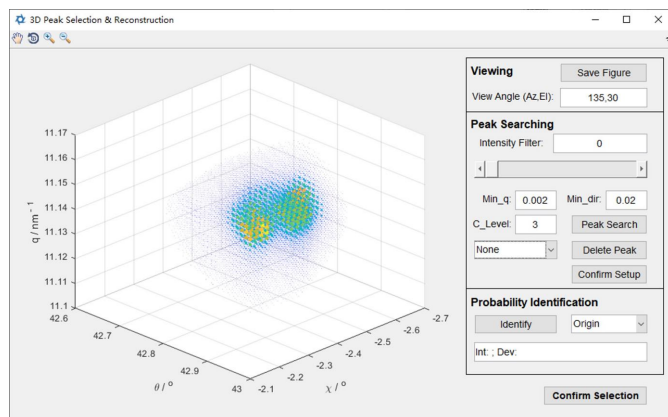


Figure 9
3D peak profile reconstruction of the energy scan data taken at the interdendritic region of a Ni-based superalloy. The pair of partially overlapped peaks indicates slightly misoriented adjacent dendrites.

dimensions. As Fig. 9 shows, a Cartesian coordinate system, θ – χ – q , is established to visualize the 3D peak profile. By definition, 2θ and χ are employed to define the direction of the scattering vector \mathbf{k} of each pixel, where

$$\begin{cases} \theta = \frac{1}{2} \cos^{-1}(\mathbf{k} \cdot \mathbf{k}_{in}), \\ \chi = -\tan^{-1}([\mathbf{k}]_1/[\mathbf{k}]_3). \end{cases} \quad (8)$$

The subscripts 1 and 3 mean the first and third components of the \mathbf{k} vector. The length of the \mathbf{k} vector is quantified by q , which is defined as $q = [(2E)/(hc)] \sin \theta$, where E is the energy of the X-ray beam, h is Planck's constant and c is the speed of light. Then each pixel on the energy scan pattern is converted into a dot in Fig. 9. The intensity of this pixel is illustrated by false colors, with blue the lowest and red the highest. Note that, in the solid-state physics literature, q is usually defined as $q = [(4\pi E)/(hc)] \sin \theta$. If this terminology is utilized, a factor of 2π must be incorporated into the calculations.

Fig. 10 demonstrates the reconstructed peak profile in three dimensions from an energy scan data set, obtained from the interdendrite region of a Ni-based superalloy. Considering that the synchrotron X-ray beam with an energy of ~ 10 keV has been focused to the submicrometre scale, the two partially overlapped peaks observed in the energy scan data set are obtained from two slightly misoriented adjacent dendrite crystals, lying in the penetration path (approximately $5 \mu\text{m}$ deep) of the X-ray beam. To analyze them further, the peaks need to be separated. *PYXIS* achieves this by employing the well developed Gaussian mixture model and expectation maximization (GMM-EM) algorithm (Xuan *et al.*, 2001). Firstly, both peaks are identified using the method introduced in Section 3.2.3 (except in three dimensions) and marked by brown boxes [Fig. 10(a)]. Within the brown boxes, each peak is fitted using a 3D Gaussian model and the parameters like peak center and peak width are input as the starting point of GMM-EM fitting, until the deviation between the fitted intensity and the correlated observed value converges to a constant. Then,

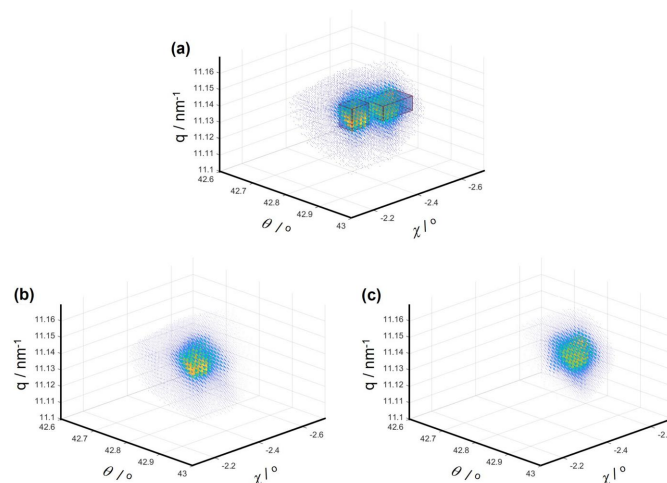


Figure 10
Separation of partially overlapped reconstructed peaks. (a) Peak position identification, highlighted by brown boxes. (b)–(c) Peak separation by applying the Gaussian mixture model and expectation maximization (GMM-EM) algorithm.

the profile of each individual peak is separated and displayed as in Figs. 10(b) and 10(c).

3.4.2. Lattice misfit measurement. The reconstructed 3D peak profile can be applied to measure the lattice misfit between matrix and precipitates in Ni-based superalloys and other materials with coherent or semi-coherent precipitates. First, the 3D peak profile is projected onto the q axis by integrating the intensities over both θ and χ axes to obtain the q profile. In Fig. 11, an asymmetric peak q profile is derived from the peak in Fig. 10(b) (blue dots). Then, the q profile is decomposed by fitting the two subpeaks following the pseudo-Voigt distribution:

$$I = s[wG'_{(x,\sigma)} + (1-w)L'_{(x,\sigma)}], \quad (9)$$

Here, I is the intensity, s and w are the scaling and weighting coefficients, and $G'_{(x,\sigma)}$ and $L'_{(x,\sigma)}$ are similar to the Gaussian and Lorentzian distributions:

$$G'_{(x,\sigma)} = \frac{2\sqrt{\ln 2}}{\pi\sigma} \exp\left[-\frac{4\ln 2}{\sigma^2}(q - q_c)^2\right], \quad (10)$$

$$L'_{(x,\sigma)} = \frac{2}{\pi} \frac{\sigma}{4(q - q_c)^2 + \sigma^2}. \quad (11)$$

σ is the fitted FWHM of the subpeak, and q_c defines the peak center. To accelerate the fitting process, users are required to input the rough peak center positions into *PYXIS* using the box to the left side of the interface (highlighted by the dashed brown box).

In Fig. 11, the profiles of the two fitted subpeaks, as well as their sum, are overlaid on the q profile as red, yellow and blue curves, respectively. To check the accuracy of the decomposition, the intensity discrepancies between the experimental and fitted values are shown below. Additionally, the volume fractions of both phases can be calculated from the integrated areas of the subpeaks. In this case, the volume fraction of the

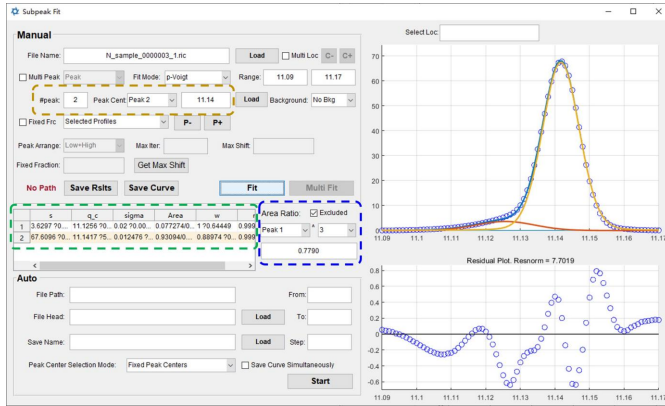


Figure 11
The interface for q -profile analysis, enabling lattice constant and lattice misfit measurement.

precipitate is estimated to be $\sim 78\%$ (displayed in the dashed blue box). As a cross check, the same sample is characterized using a scanning electron microscope and the precipitate volume fraction is measured using the software package *Image-J*. The result, 76% , is consistent with the energy scan data. This also validates the accuracy of the subpeak decomposition.

More information about the two subpeaks is given in the table in the dashed green box, including the parameters s , q_c , σ and w . The lattice constants of the precipitates and matrix can be derived from the peak centers by applying the equation $a = \sqrt{h^2 + k^2 + l^2}/q_c$, where h , k and l are the Miller indices of the diffraction peak. The lattice misfit between the matrix and the precipitates is then computed from

$$\Delta = \frac{2(a_p - a_m)}{a_p + a_m}, \quad (12)$$

where a_m and a_p are the lattice constants of the matrix and precipitates, respectively. In this example, a_p and a_m are measured to be 0.3590 and 0.3595 nm, and the lattice misfit is -1.4×10^{-3} , which is of the same magnitude as the previously reported results for Ni-based superalloys (Brückner *et al.*, 1997).

3.4.3. Dislocation characterization. The method developed by Wilkens allows dislocation characterization based on the q profiles (Wilkens, 1969, 1970). In Wilkens's model, the q profile is described by the following equations:

$$I(q) = \int_0^{+\infty} A(n) \cos\left(\frac{2\pi n q}{\sqrt{\rho}}\right) dn, \quad (13)$$

$$A(n) = \exp\left(-\frac{1}{8\pi} Q_0^2 b^2 C n^2 f(\eta)\right), \quad (14)$$

$$f(\eta) = \begin{cases} -\ln(\eta) + \frac{7}{4} - \ln(2) + \frac{512}{90\pi\eta} \\ + \frac{2}{\pi} \left(1 - \frac{1}{4\eta^2}\right) \int_0^V \frac{\sin^{-1}(V)}{V} dV \\ + \frac{\eta^2}{6} - \left(\frac{769}{180\eta} + \frac{41\eta}{90} + \frac{2\eta^3}{90}\right) \frac{\sqrt{1-\eta^2}}{\pi} \\ - \left(\frac{11}{12\eta^2} + \frac{7}{2} + \frac{\eta^3}{3}\right) \frac{\sin^{-1}(\eta)}{\pi}, & \eta \in (0, 1), \\ \frac{512}{90\pi\eta} - \frac{11 + 6\ln(2\eta)}{24\eta^2}, & \eta \in [1, +\infty), \end{cases} \quad (15)$$

$$n \simeq \frac{2M}{\exp(0.7)\sigma\mu} \eta, \quad (16)$$

where ρ is the dislocation density, Q_0 the length of the scattering vector, b the length of the Burgers vector, C the orientation constant, and σ and μ parameters to describe the orientation of the scattering vector with respect to the dislocation line direction and Burgers vector, respectively. $f(\eta)$ is a complex function defined by Wilkens. More details on the calculation of σ , μ and the orientation constant C are provided in Appendix C.

Fitting the q profile with equations (13) and (14) helps in determining the dislocation density ρ and the effective outer cut-off radius R_c , but the integration consumes considerable time owing to the complexity of the $f(\eta)$ function. Our research team has tried to simplify the fitting process by deriving the dislocation screening factor M first (Zhou *et al.*, 2021). However, this strategy is not implementable using computer algorithms. Hence, *PYXIS* utilizes the Taylor series to simplify the calculation of equations (13) and (14) by rewriting them as follows:

$$I(q) = \int_0^{+\infty} A(n) \cos(t_2 q n) dn, \quad (17)$$

$$A(n) = \exp(t_1 n^2 f(\eta)), \quad (18)$$

where

$$t_1 = -\frac{Q_0^2 b^2 C M^2}{2\pi \exp(1.4)\sigma^2 \mu^2}, \quad (19)$$

$$t_2 = \frac{2M}{\exp(0.7)\mu\sigma\sqrt{\rho}}. \quad (20)$$

Then, the integration of equation (15) will be performed in the η ranges of $(0, 1)$ and $[1, +\infty)$, respectively.

First, in the range $\eta \in (0, 1)$, $\eta^2 f(\eta)$ is transferred into its fourth-order Taylor expansion at $\eta = 0.5$, which introduces a marginal discrepancy of 0.003 from the numerically computed value, obtained from the original equation. Thus, equation (17) is rewritten as

$$I_{(q)} = \int_0^1 \exp[t_1 P_{4(\eta)}] \cos(t_2 q \eta) d\eta, \quad (21)$$

where $P_{4(\eta)}$ is obtained from the fourth-order Taylor series fitting, which equals

$$P_{4(\eta)} = 0.55709\eta^4 - 1.68062\eta^3 + 2.11257\eta^2 + 0.19606\eta - 0.00419. \quad (22)$$

Thus, in the range $\eta \in (0, 1)$, equation (21) becomes a numerical integral, which always takes less than 1 s on an ordinary personal computer.

In the range $\eta \in [1, +\infty)$, equation (18) can be significantly simplified into the following:

$$A_{(\eta)} = \exp\left[t_1 \left(\frac{512}{90\pi}\eta - \frac{\ln(2\eta)}{4} - \frac{11}{24}\right)\right]. \quad (23)$$

Then $\eta^2 f_{(\eta)}$ is written using the Taylor series, and fitted in the range of $[1, 1.5]$ using the first-order Taylor expansion at 1.25. As Fig. 12 shows, the fit is good and the discrepancy between the Taylor series fitting and the original formula calculation is always less than 0.006. Since $\eta^2 f_{(\eta)}$ is the difference between a linear function $[(512/90\pi)\eta - (11/24)]$ and a logarithm function $[\ln(2\eta)/4]$, as η increases, its first-order Taylor expansion is closer to its true value. Thus, in the range $[1, +\infty)$, equation (17) is converted into

$$I_{(q)} = \sum_{i=1}^{+\infty} \int_{0.5i-0.5}^{0.5i+1} \exp[t_1 P_{1(0.5i+0.75, \eta)}] \cos(t_2 q \eta) d\eta, \quad (24)$$

where $P_{1(\alpha, \eta)}$ is the first-order Taylor expansion of $\eta^2 f_{(\eta)}$ at α .

Since t_1 is less than 0, $A_{(\eta)}$ approaches 0 as η increases. Practically, the sum will stop when $A_{(\eta)}$ is less than 0.0001. Additionally, $I_{(q)}$ has an analytical solution when $\eta^2 f_{(\eta)}$ is replaced by its first-order Taylor series. Thus, in the range $[1, +\infty)$, equation (24) is calculated without an integral.

An example of dislocation density characterization based on the Wilkens method is demonstrated here. The q profiles of the γ phase in the deformed (deformation condition explained in Appendix A) and dislocation-free (fully annealed at 1290°C for 3 h and then 1300°C for 6 h) states are demonstrated in Figs. 13(a) and 13(b), respectively. The q profile obtained from the dislocation-free specimen is likely to arise from the instrumental broadening effect. This could be attributed to the divergence of the micro/nanofocused X-ray beam, or the detector broadening and the size effect of the γ phase in

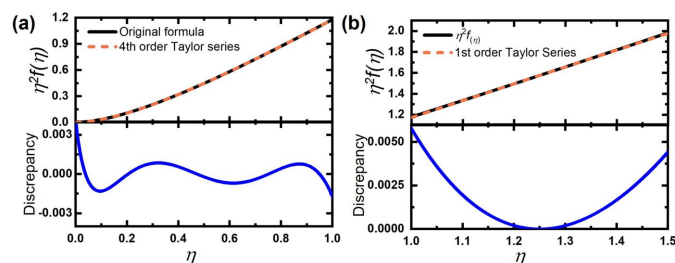


Figure 12
 $\eta^2 f_{(\eta)}$ fitting in the range of (a) $\eta \in (0, 1)$ and (b) $\eta \in [1, +\infty)$.

superallloys. Thus the dislocation-induced q -profile broadening is calculated by deconvoluting the instrumental broadening (obtained from the annealed alloy) from the deformed profile by applying equations (25)–(28), as displayed in Fig. 13(c),

$$A_{\text{def}}(n) = \int_{-\infty}^{+\infty} I_{\text{def}}(q) \exp(2\pi n q i) dq, \quad (25)$$

$$A_{\text{annealed}}(n) = \int_{-\infty}^{+\infty} I_{\text{annealed}}(q) \exp(2\pi n q i) dq, \quad (26)$$

$$A_{\text{decon}}(n) = A_{\text{def}}(n)/A_{\text{annealed}}(n), \quad (27)$$

$$I_{\text{decon}}(q) = \int_{-\infty}^{+\infty} A_{\text{decon}}(n) \exp(-2\pi n q i) dn. \quad (28)$$

Here the subscripts def, annealed and decon refer to the states of deformed, annealed and deconvoluted, respectively.

Consequently, by applying equations (17)–(24), the deconvoluted q profile can be fitted within a couple of seconds. This function is performed on the interface as shown in Fig. 13(d). *PYXIS* calculates the orientation constant, C , as well as σ and μ , based on the selected dislocation types and their fractions automatically (displayed on the left side). Since the Wilkens model requires the q profile to be symmetric, only the right half of it is displayed in blue dots on the right panel of the interface. The red curve represents the fitting result, and the discrepancy between experimental and fitting data is plotted below. The values of M , dislocation density ρ and effective

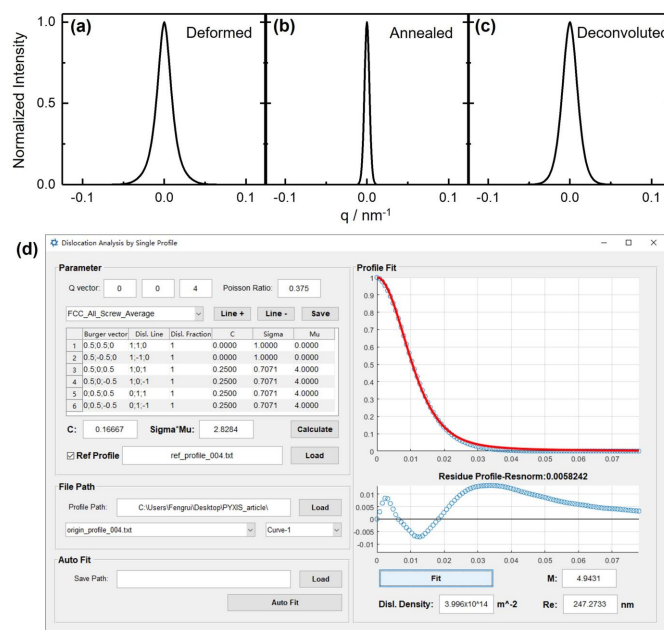


Figure 13
Dislocation characterization based on the Wilkens model. The q profiles of the deformed (a), annealed (b) and deconvoluted (c) superallloys are obtained from the peak reconstructions. (d) Dislocation densities are calculated and displayed on the *PYXIS* interface.

outer cut-off radius R_e are the output in the bottom right corner.

4. Conclusions and outlook

In this article, we have described the main functions of *PYXIS*, a comprehensive software package dedicated to processing micro-Laue and energy scan diffraction data. *PYXIS* enables efficient analysis of Laue patterns with zone-axis assisted indexing and a peak position comparison strategy. It also allows the reconstruction of peak profiles in 3D reciprocal space from the energy scan data, which can be further applied to measure the lattice constants, lattice misfit and dislocation characteristics. Other functions not covered in this article can be found in the user manual.

We plan to upgrade *PYXIS* in response to users' feedback. Some potential improvements include (i) incorporating deep learning methods for indexing Laue patterns, in addition to the machine learning algorithms, to achieve higher efficiency; (ii) developing more image recognition algorithms for peak identification, especially for materials with high defect density that produce low-quality Laue patterns.

APPENDIX A

Sample preparation

A1. Garnet-type $\text{Li}_7\text{La}_3\text{Zr}_2\text{O}_{12}$ (LLZO)

LLZO powder was synthesized via a solid-state reaction as described in detail elsewhere (Shen *et al.*, 2022). The powder was cold pressed without binder into 11 mm-diameter pellets. The green pellets were covered with fresh LLZO powder and sintered at 1150°C for 8 h in an argon atmosphere. The surfaces of the sintered pellets were cleaned and polished with sandpaper to remove any surface impurities. Then, the pellet disc was halved using a diamond saw and the cross section was polished with sandpaper. The semicircular pellet was assembled into a Li/LLZO/Li cell and fixed in a sealed sample stage. The lithium tabs were aligned with the polished LLZO cross section and positioned to face the X-ray window which was covered by Kapton tape.

A2. Ni-based superalloy single crystal

A cylindrical CMSX-4 Ni-based superalloy single-crystal specimen was cut from a cast [001] boule. To eliminate the eutectic phase, the sample underwent a two-step solution treatment at 1290°C for 3 h and then 1300°C for 6 h, following aging annealing at 1140°C for 2 h and 870°C for 20 h, and was finally air cooled to ambient temperature. The surface was electro-polished in 10% perchloric acid alcohol solution at a voltage of 25 V for about 15 s. The cross-shaped dendrites were visible under secondary electron imaging mode in a scanning electron microscope after etching in 0.2 g ml⁻¹ FeCl₃ and 14% hydrochloric acid solution for about 5 s [see Fig. 14(a)]. The position of the energy scan is marked by the red arrow. Then, the surface was electro-polished again by the method described above for microdiffraction. The

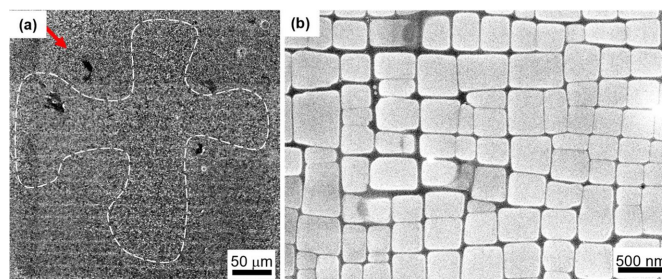


Figure 14

The cross-shaped dendrites (a) and the morphology at the energy scan position (b).

morphology at the energy scan position was investigated by scanning electron microscopy [Fig. 14(b)].

The deformed superalloy sample was vibration fatigued using a D-300 vibrating machine from the Suzhou SuShi Testing Group Co. Ltd, according to the standard of the Ministry of the Aviation Industry of China (HB5277-84). Afterwards it was cut and polished in a similar way to the heat-treated sample.

APPENDIX B

Strain refinement algorithm

The deviatoric lattice strain tensor is obtained in the following way. For each pair of indexed peaks, the angle between their scattering vectors ($\delta_{e,ij}$) is calculated:

$$\delta_{e,ij} = \cos^{-1} \left[\frac{(\mathbf{k}_i - \mathbf{k}_{in}) \cdot (\mathbf{k}_j - \mathbf{k}_{in})}{|\mathbf{k}_i - \mathbf{k}_{in}| \cdot |\mathbf{k}_j - \mathbf{k}_{in}|} \right]. \quad (29)$$

In the crystal Cartesian coordinate system, the scattering vector of peak i can be calculated using equations (30)–(32):

$$\mathbf{k}_{t,i} = \mathbf{M} \begin{bmatrix} h_i \\ k_i \\ l_i \end{bmatrix}, \quad (30)$$

$$\mathbf{M} = \begin{bmatrix} a \sin \beta & bq \sin \alpha & 0 \\ 0 & b\sqrt{1-q^2} \sin \alpha & 0 \\ a \cos \beta & b \cos \alpha & c \end{bmatrix}, \quad (31)$$

$$q = \frac{\cos \gamma - \cos \alpha \cos \beta}{\sin \alpha \sin \beta}, \quad (32)$$

where the subscript t in $\mathbf{k}_{t,i}$ denotes the theoretical value and the matrix \mathbf{M} is a transfer matrix converting the Miller indices into the Cartesian coordinates. Thus, the theoretical angle between scattering vectors i and j , denoted as $\delta_{t,ij}$, can be computed using equation (33):

$$\delta_{t,ij} = \cos^{-1} \left(\frac{\mathbf{k}_{t,i} \cdot \mathbf{k}_{t,j}}{|\mathbf{k}_{t,i}| \cdot |\mathbf{k}_{t,j}|} \right). \quad (33)$$

A list of both $\delta_{e,ij}$ and their theoretical values $\delta_{t,ij}$ is then input into the Nelder–Mead simplex optimization process. This process iteratively adjusts the lattice constants to minimize the

difference between $\delta_{e,ij}$ and $\delta_{t,ij}$ until the difference converges to a stable point.

Once such convergence is achieved, the strained lattice constants are determined. Transfer matrices \mathbf{M}_s and \mathbf{M}_0 are then calculated from the strained and strain-free lattice constants. Subsequently, the strain tensor is derived from these two matrices through equations (34) and (35):

$$\varepsilon = \frac{1}{2}(\mathbf{S} + \mathbf{S}^T) - \mathbf{I}, \quad (34)$$

$$\mathbf{S} = \mathbf{M}_s(\mathbf{M}_0)^{-1}. \quad (35)$$

The dilatational and deviatoric components are decoupled in the strain tensor ε by applying equation (36):

$$\varepsilon_{\text{dev}} = \begin{bmatrix} \varepsilon_{11} - \Delta & \varepsilon_{12} & \varepsilon_{13} \\ \varepsilon_{21} & \varepsilon_{22} - \Delta & \varepsilon_{23} \\ \varepsilon_{31} & \varepsilon_{32} & \varepsilon_{33} - \Delta \end{bmatrix}, \quad (36)$$

where $\Delta = (1/3)(\varepsilon_{11} + \varepsilon_{22} + \varepsilon_{33})$.

Finally, the deviatoric strain tensor is converted from the crystal Cartesian coordinate system into the sample coordinate system:

$$\varepsilon_{\text{dev}}^{\text{sample}} = \mathbf{R}_{\text{ori}} \varepsilon_{\text{dev}} \mathbf{R}_{\text{ori}}^{-1}, \quad (37)$$

where the rotation matrix \mathbf{R}_{ori} is determined by the local crystal orientation.

APPENDIX C

Calculation of σ , μ and the orientation constant C

For a given dislocation system with a certain Burgers vector (\mathbf{b}) and dislocation line direction (\mathbf{l}), the parameters σ and μ can be calculated using the following equations:

$$\sigma = \frac{|\mathbf{Q}_0 \times \mathbf{l}|}{|\mathbf{Q}_0| |\mathbf{l}|}, \quad (38)$$

$$\mu = \frac{|\mathbf{Q}_0| |\mathbf{b}|}{2\pi}, \quad (39)$$

where \mathbf{Q}_0 is the scattering vector.

The orientation constant C is calculated as follows:

$$C = \sin^2 \gamma_d C_{\text{ed}} + \cos^2 \gamma_d C_{\text{sd}} + \sin \gamma_d \cos \gamma_d C_{\text{md}}, \quad (40)$$

where γ_d is the angle between the Burgers vector \mathbf{b} and dislocation line direction \mathbf{l} .

C_{ed} , C_{sd} and C_{md} are the orientation constants of edge, screw and mixed dislocations, which are expressed as

$$C_{\text{ed}} = \frac{\sin^4 \psi_d [1 - 4\nu + 8\nu^2 + 4(1 - 2\nu) \cos^2 \phi_d]}{8(1 - \nu)^2}, \quad (41)$$

$$C_{\text{sd}} = \sin^2 \psi_d \cos^2 \psi_d, \quad (42)$$

$$C_{\text{md}} = \frac{\sin^3 \psi_d \cos \psi_d \cos \phi_d (3 - 7\nu + 4\nu^2)}{2(1 - \nu)^2}, \quad (43)$$

where ν is the Poisson ratio. ψ_d and ϕ_d are calculated by

$$\psi_d = \cos^{-1} \left(\frac{\mathbf{Q}_0 \cdot \mathbf{l}}{|\mathbf{Q}_0| |\mathbf{l}|} \right), \quad (44)$$

$$\phi_d = \sin^{-1} \left(\frac{\mathbf{Q}_0 \times \mathbf{l} \cdot \mathbf{b}}{|\mathbf{Q}_0| |\mathbf{l}| |\mathbf{b}| \sin \psi_d} \right). \quad (45)$$

Practically, several dislocation systems exist simultaneously. We assume there are n types of dislocation systems and the i th type exhibits a fraction of f_i . The average orientation constant C^* is $\sum_{i=1}^n f_i C_i$. The averages σ^* and μ^* are $\prod_{i=1}^n \sigma_i^{(C_i/C^*)f_i}$ and $\prod_{i=1}^n \mu_i^{(C_i/C^*)f_i}$, respectively.

Acknowledgements

We appreciate the support of the International Joint Laboratory for Micro/Nano Manufacturing and Measurement Technologies. We thank the Instrumental Analysis Center of Xi'an Jiaotong University and Dr Chuanwei Fan from CAMPNano for technical support. We also acknowledge helpful discussions with Professor R. Lakshmi Narayan from the Indian Institute of Technology, Delhi.

Funding information

The following funding is acknowledged: National Natural Science Foundation of China (grant Nos. 51927801, U2032205, 52271042); 111 Project 2.0 (grant No. BP0618008).

References

- Arce, G. & McLoughlin, M. (1987). *IEEE Trans. Acoust. Speech Signal. Process.* **35**, 60–69.
- Ballard, D. H. (1981). *Pattern Recognit.* **13**, 111–122.
- Befus, K. S., Manga, M., Stan, C. & Tamura, N. (2019). *Geophys. Res. Lett.* **46**, 8791–8800.
- Brückner, U., Epishin, A. & Link, T. (1997). *Acta Mater.* **45**, 5223–5231.
- Chen, K., Dejoie, C. & Wenk, H.-R. (2012). *J. Appl. Cryst.* **45**, 982–989.
- Chen, K., Huang, R., Li, Y., Lin, S., Zhu, W., Tamura, N., Li, J., Shan, Z. W. & Ma, E. (2020). *Adv. Mater.* **32**, 1907164.
- Chen, K., Kunz, M., Tamura, N. & Wenk, H.-R. (2011). *Phys. Chem. Miner.* **38**, 491–500.
- Chen, K., Kunz, M., Tamura, N. & Wenk, H.-R. (2015). *Geology*, **43**, 219–222.
- Chung, J.-S. & Ice, G. E. (1999). *J. Appl. Phys.* **86**, 5249–5255.
- Dejoie, C., Sciau, P., Li, W., Noé, L., Mehta, A., Chen, K., Luo, H., Kunz, M., Tamura, N. & Liu, Z. (2014). *Sci. Rep.* **4**, 4941.
- Guo, H., Chen, K., Oh, Y., Wang, K., Dejoie, C., Syed Asif, S., Warren, O., Shan, Z., Wu, J. & Minor, A. (2011). *Nano Lett.* **11**, 3207–3213.
- Ice, G. & Barabash, R. (2007). *Dislocations in Solids*, Vol. 13, pp. 499–601. Amsterdam: Elsevier.
- Ice, G. E., Budai, J. D. & Pang, J. W. (2011). *Science*, **334**, 1234–1239.
- Ice, G. E., Larson, B. C., Yang, W., Budai, J. D., Tischler, J. Z., Pang, J. W. L., Barabash, R. I. & Liu, W. (2005). *J. Synchrotron Rad.* **12**, 155–162.
- Kou, J., Chen, K. & Tamura, N. (2018). *Scr. Mater.* **143**, 49–53.
- Levine, L. E., Larson, B. C., Yang, W., Kassner, M. E., Tischler, J. Z., Delos-Reyes, M. A., Fields, R. J. & Liu, W. (2006). *Nat. Mater.* **5**, 619–622.

- Li, Y., Chen, K., Dang, X., Zhang, F., Tamura, N., Ku, C.-S., Kang, H. & Wenk, H.-R. (2020). *J. Appl. Cryst.* **53**, 1392–1403.
- Li, Y., Wan, L. & Chen, K. (2015). *J. Appl. Cryst.* **48**, 747–757.
- Liu, W., Ice, G. E., Larson, B. C., Yang, W., Tischler, J. Z. & Budai, J. D. (2004). *Metall. Mater. Trans. A*, **35**, 1963–1967.
- Ma, E. Y., Cui, Y.-T., Ueda, K., Tang, S., Chen, K., Tamura, N., Wu, P. M., Fujioka, J., Tokura, Y. & Shen, Z.-X. (2015). *Science*, **350**, 538–541.
- Mun, B. S., Chen, K., Yoon, J., Dejoie, C., Tamura, N., Kunz, M., Liu, Z., Grass, M. E., Mo, S.-K., Park, C., Lee, Y. Y. & Ju, H. (2011). *Phys. Rev. B*, **84**, 113109.
- Ohashi, T., Barabash, R. I., Pang, J., Ice, G. E. & Barabash, O. M. (2009). *Int. J. Plast.* **25**, 920–941.
- Olsson, D. M. & Nelson, L. S. (1975). *Technometrics*, **17**, 45–51.
- Örs, T., Micha, J.-S., Gey, N., Michel, V., Castelnau, O. & Guinebre-
tiere, R. (2018). *J. Appl. Cryst.* **51**, 55–67.
- Purushottam Raj Purohit, R. R. P., Tardif, S., Castelnau, O., Eymery, J., Guinebre-
tiere, R., Robach, O., Ors, T. & Micha, J.-S. (2022). *J. Appl. Cryst.* **55**, 737–750.
- Robach, O., Kirchlechner, C., Micha, J. S., Ulrich, O., Biquard, X., Geaymond, O., Castelnau, O., Bornert, M., Petit, J. & Berveiller, S. (2014). *Strain and Dislocation Gradients from Diffraction: Spatially Resolved Local Structure and Defects*, pp. 156–204. Singapore: World Scientific.
- Shen, H., Chen, K., Kou, J., Jia, Z., Tamura, N., Hua, W., Tang, W., Ehrenberg, H. & Doeffer, M. (2022). *Mater. Today*, **57**, 180–191.
- Tamura, N. (2014). *Strain and Dislocation Gradients from Diffraction: Spatially Resolved Local Structure and Defects*, pp. 125–155. Singapore: World Scientific.
- Tao, X., Lv, G.-C., Kou, J., Xiong, X., Volinsky, A. A., Ku, C.-S., Chen, K. & Su, Y.-J. (2019). *Scr. Mater.* **169**, 82–86.
- Wenk, H.-R., Chandler, B. C., Chen, K., Li, Y., Tamura, N. & Yu, R. (2020). *Geophys. J. Int.* **222**, 1363–1378.
- Wenk, H.-R., Chen, K. & Smith, R. (2011). *Am. Mineral.* **96**, 1316–1324.
- Wilkins, M. (1969). *Acta Metall.* **17**, 1155–1159.
- Wilkins, M. (1970). *Phys. Status Solidi A*, **2**, 359–370.
- Xuan, G., Zhang, W. & Chai, P. (2001). *Proceedings of the 2001 International Conference on Image Processing* (Cat. No. 01CE37205), pp. 145–148. New York: IEEE.
- Yu, S., Schmidt, R. D., Garcia-Mendez, R., Herbert, E., Dudney, N. J., Wolfenstine, J. B., Sakamoto, J. & Siegel, D. J. (2016). *Chem. Mater.* **28**, 197–206.
- Zhou, G., Pantleon, W., Xu, R., Liu, W., Chen, K. & Zhang, Y. (2021). *Mater. Res. Lett.* **9**, 182–188.